



First Observation of the MeV Gamma-Ray Universe with Bijective Imaging Spectroscopy Using the Electron-tracking Compton Telescope on Board SMILE-2+

Atsushi Takada¹ , Taito Takemura¹, Kei Yoshikawa¹, Yoshitaka Mizumura² , Tomonori Ikeda¹, Yuta Nakamura¹, Ken Onozaka¹, Mitsuru Abe¹, Kenji Hamaguchi³ , Hidetoshi Kubo¹ , Shunsuke Kurosawa⁴ , Kentaro Miuchi⁵ , Kaname Saito¹, Tatsuya Sawano⁶ , and Toru Tanimori¹

¹ Graduate School of Science, Kyoto University Kitashirakawa Oiwakecho, Sakyo, Kyoto, Kyoto, 606-8502, Japan; takada@cr.scphys.kyoto-u.ac.jp

² Institute of Space and Astronautical Science, Japan Aerospace Exploration Agency Yoshinodai 3-1-1, Chuo, Sagami, Kanagawa, 252-5210, Japan

³ Department of Physics, University of Maryland, Baltimore County 1000 Hilltop Circle, Baltimore, MD 21250, USA

⁴ Institute of Materials Research, Tohoku University Katahira 2-1-1, Aoba, Sendai, Miyagi, 980-8577, Japan

⁵ Graduate School of Science, Kobe University 1-1 Rokkoudai-cho, Nada-ku, Kobe, Hyogo, 657-8501, Japan

⁶ Graduate School of Natural Science and Technology, Kanazawa University Kakuma, Kanazawa, Ishikawa, 920-1192, Japan

Received 2021 June 30; revised 2022 March 10; accepted 2022 March 23; published 2022 April 28

Abstract

MeV gamma-rays provide a unique window for the direct measurement of line emissions from radioisotopes, but observations have made little significant progress since COMPTEL on board the Compton Gamma-ray Observatory (CGRO). To observe celestial objects in this band, we are developing an electron-tracking Compton camera (ETCC) that realizes both bijective imaging spectroscopy and efficient background reduction gleaned from the recoil-electron track information. The energy spectrum of the observation target can then be obtained by a simple ON–OFF method using a correctly defined point-spread function on the celestial sphere. The performance of celestial object observations was validated on the second balloon SMILE-2+ , on which an ETCC with a gaseous electron tracker was installed that had a volume of $30 \times 30 \times 30 \text{ cm}^3$. Gamma-rays from the Crab Nebula were detected with a significance of 4.0σ in the energy range 0.15–2.1 MeV with a live time of 5.1 hr, as expected before launch. Additionally, the light curve clarified an enhancement of gamma-ray events generated in the Galactic center region, indicating that a significant proportion of the final remaining events are cosmic gamma-rays. Independently, the observed intensity and time variation were consistent with the prelaunch estimates except in the Galactic center region. The estimates were based on the total background of extragalactic diffuse, atmospheric, and instrumental gamma-rays after accounting for the variations in the atmospheric depth and rigidity during the level flight. The Crab results and light curve strongly support our understanding of both the detection sensitivity and the background in real observations. This work promises significant advances in MeV gamma-ray astronomy.

Unified Astronomy Thesaurus concepts: [Gamma-ray astronomy \(628\)](#); [Gamma-ray observatories \(632\)](#); [Gamma-ray detectors \(630\)](#); [Gamma-ray telescopes \(634\)](#); [High altitude balloons \(738\)](#)

1. Introduction

Various radiation process in the universe can be observed in the low-energy gamma-ray band (0.1–100 MeV). Examples are line emissions from the radioisotopes produced by nucleosynthesis in supernovae or neutron star mergers (Matz et al. 1988; von Ballmoos 1995), the electron–positron annihilation line in the Galactic center region (GCR; Prantzos et al. 2011), synchrotron emissions and inverse Compton scattering with particle acceleration in active galactic nuclei or gamma-ray bursts (GRBs; Urry & Padovani 1995; Briggs et al. 1999), pion-decay radiation in the strong gravity fields around black holes (McConnell et al. 1996; Mahadevan et al. 1997), and de-excitation lines from nuclei excited by interactions between cosmic rays and the interstellar medium (Boggs et al. 2000; Strong et al. 2000). Population III stars are expected to be detected as long-duration GRBs (Mészáros & Rees 2010; Toma et al. 2011) because the universe is very transparent in this energy band. Thermal emissions in the extragalactic diffuse emission might confirm the existence of primordial black holes

(PBHs) with masses of 10^{16-17} g , which emit thermal emission in the MeV band (Carr et al. 2010).

Although celestial MeV gamma-rays have been observed since the dawn of high-energy astrophysics, when GRBs were discovered by Vela and extragalactic diffuse emission was detected by Apollo 15 (Trombka et al. 1973), observations in this band stagnate. COMPTEL on board the Compton Gamma-ray Observatory (CGRO; Schönfelder et al. 1993) discovered only ~ 30 steady gamma-ray sources in the 0.75–30 MeV band (Schönfelder et al. 2000), and the Spectrometer on board INTEGRAL (SPI) discovered only four steady celestial objects at energies above 0.6 MeV (Bouchet et al. 2008). The expected signatures of supernova explosions are line gamma-rays emitted from fresh isotopes, but line gamma-rays of $^{56}\text{Ni}/^{56}\text{Co}$ have been detected only from SN1987A (Matz et al. 1988) and SN2014J (Diehl et al. 2015; Churazov et al. 2015). Various gamma-ray telescopes are being developed and some balloon experiments have been performed, but none of the present developments have surpassed the sensitivity of COMPTEL (Aprile et al. 2008; Bandstra et al. 2011; Kamiya 2011). The Nuclear Compton Telescope (NCT; predecessor of the Compton Spectrometer and Imager, COSI) produced some observational results using a wide-view Ge Compton camera loaded on a few balloon experiments. In

Original content from this work may be used under the terms of the [Creative Commons Attribution 4.0 licence](#). Any further distribution of this work must maintain attribution to the author(s) and the title of the work, journal citation and DOI.

2009, COSI detected Crab at the 4σ (Bandstra et al. 2011) significance level. In 2016, they detected the annihilation line from GCR at the 7σ significance level (Kierans et al. 2020; Siebert et al. 2020).

MeV observations have been bottlenecked by the huge background and difficulty of imaging. Unlike visible light or X-rays, MeV gamma-ray wavelengths are too short to focus by a mirror or lens. Obtaining their total energy is also difficult because whereas most incident photons deposit only part of their energy via Compton scattering, Compton scattering dominates the interactions between MeV gamma-rays and materials. In addition, observations are obstructed by huge numbers of background photons produced by hadronic interactions between cosmic rays and the material surrounding the detector (Weidenspointner et al. 2001). The SPI and other detectors based on coded aperture imaging infer the intensity map of incident gamma-rays from the pattern of the shadow image. These detectors need many photons to obtain the directions of celestial objects. Coded aperture imaging telescopes are usually equipped with an active veto counter, but heavy anticoincidence counters scarcely improve the signal-to-noise ratio because the gamma-rays produced by cosmic rays are delayed (Diehl et al. 2018). Conventional Compton cameras such as COMPTEL can slightly suppress the contaminating background photons by partially restricting the incident direction of each photon. However, this type of camera measures only one of two angles representing the direction of incident gamma-rays due to the lack of recoil direction. The signal-to-noise ratio depends on the volume of the cone-shape response in the Compton data space (Schönfelder et al. 1993), in which the information of recoil directions degenerates. Therefore, the observations are obstructed by large contamination of gamma-rays within the area spanned by a radius defined by the average of the detectable scattering angle. The detection sensitivity of a nonbijection telescope based on coded aperture imaging or conventional Compton imaging is inherently restricted by the principle confusion limit caused by the overlapped responses of the surrounding sources. In fact, Schönfelder (2004) argued that above all abilities, next-generation MeV gamma-ray telescopes must distinguish and reject the background based on sharp point-spread function (PSF) on the celestial sphere and additional event-selection parameters. In early 2000, the MEGA group measured the tracks of recoil electrons with energies higher than 2 MeV using a Si-tracker and CsI calorimeters. They reported worse angular resolution measures (ARMs) of tracked events than untracked events because detecting a few sampling points of the electron track requires a high recoil energy (Zoglauer et al. 2003). Thus, a tracking detector must finely track electrons, even those with very low energies (~ 10 keV) to obtain a sufficient PSF for MeV gamma-ray astronomy.

As the next MeV gamma-ray telescope for deep sky surveying, we are developing an electron-tracking Compton camera (ETCC) that applies a gaseous electron tracker as the Compton-scattering target and pixel scintillator arrays as the absorbers (Tanimori et al. 2004). The ETCC and a conventional Compton camera differ in their tracking of Compton-recoil electrons. The ETCC obtains the momentum of an incident gamma-ray by simply summing the momenta of the scattered gamma-ray and the recoil-electron event by event. In this way, it completely reconstructs the Compton-scattering process. Thus (like other wavelength telescopes), an ETCC is a

bijection telescope, which obtains the incident direction as the zenith and azimuthal angles and forms a proper PSF on the celestial sphere. As the proper PSF defines the minimum size that conserves the intensity of gamma-rays, the spectroscopic information at many points beyond the PSF can be independently obtained from one image. Therefore, the ETCC can realize imaging spectroscopy in MeV gamma-ray astronomy. The proper PSF on the celestial sphere enables the determination of the energy spectrum of the observation target by a simple ON-OFF method (Tanimori et al. 2017). Moreover, from the recoil-electron track, the background can be rejected using two powerful tools (Tanimori et al. 2015): particle identification based on the energy deposition rate dE/dx in the gaseous electron tracker, and a Compton-scattering kinematic test based on the angle between the directions of scattered gamma-ray and recoil electron. These background-rejection tools enable ETCC observations without a heavy veto counter; consequently, the ETCC has a large field of view (FoV). These unique abilities of the ETCC provide real imaging spectroscopy to MeV gamma-ray observations. In future observations with ETCCs loaded on a satellite (Hamaguchi et al. 2019), we are planning balloon experiments, called Sub-MeV/MeV gamma-ray Imaging Loaded-on-balloon Experiments (SMILE). As the first step, we launched a small ETCC with an electron tracker with a sensitive volume of $10 \times 10 \times 15$ cm³ in 2006. This launch was intended as a background study at high altitudes (SMILE-I) and as confirmation of the background-rejection power of the ETCC (Takada et al. 2011). SMILE-I successfully detected diffuse cosmic and atmospheric gamma-rays and performed powerful background rejection based on particle identification. As the second step, SMILE was tested on imaging-spectroscopy observations of bright celestial objects. To this end, we set the Crab Nebula and GCR as the observation targets, and constructed a medium-size ETCC with a sensitive volume of $30 \times 30 \times 30$ cm³. Assuming a background of extragalactic diffuse and atmospheric gamma-rays, the Crab Nebula should be detected at the $3\text{--}5\sigma$ significance level. The second balloon, SMILE-2+, was launched at Alice Springs, Australia, on 2018 April 7.

Herein, we assess the gamma-ray detection abilities of the ETCC from ground calibrations, details of the SMILE-2+ flight, and the observation results of the Crab Nebula. We additionally discuss the detection sensitivities of the next ETCC observations by comparing the realized detection sensitivity with that estimated from ground calibrations.

2. Instruments

2.1. SMILE-2+ ETCC and Control System

At medium latitudes in the southern hemisphere, the large zenith angle ($>45^\circ$) reduces the flux of the Crab Nebula by one-half from that at low zenith angles; consequently, the air mass is twice that at the zenith. Thus, the Crab Nebula is difficult to detect even after several hours of balloon observations. To detect the Crab Nebula at the $3\text{--}5\sigma$ significance level during a few hours in the 0.2–2 MeV energy band at 40 km altitude in the southern hemisphere, the ETCC requires a minimum effective area of ~ 1 cm² (0.3 MeV). The required PSF is $\sim 30^\circ$ for 0.6 MeV detection at the half-power radius (HPR), and the instrumental background must be suppressed to below the background of the diffuse cosmic and atmospheric gamma-rays. Figure 1 is a schematic of

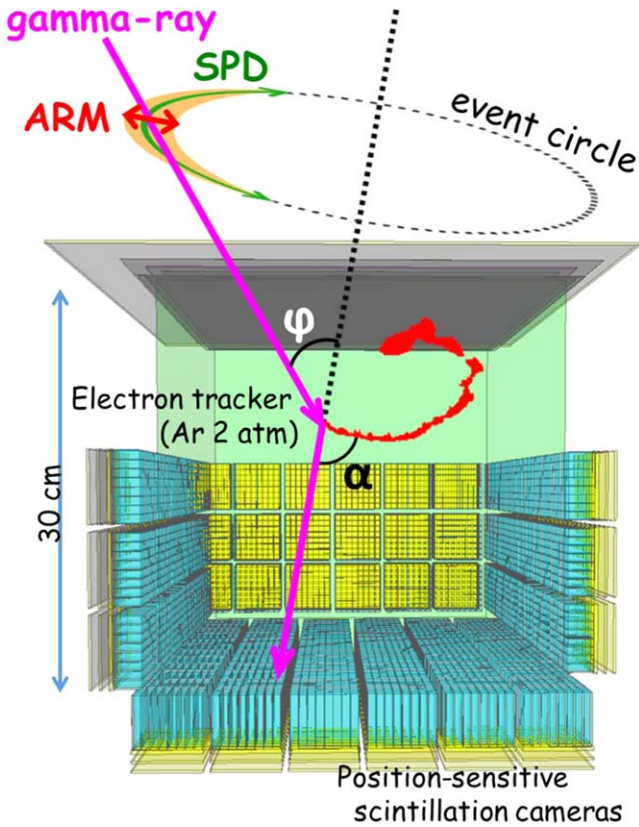


Figure 1. Schematic of the electron-tracking Compton camera (ETCC). The ETCC comprises a gaseous electron tracker as the Compton-scattering target and position-sensitive scintillation cameras that absorb the scattered gamma-rays.

SMILE-2+ ETCC. The material of a Compton-scattering target should have a high electron density to increase the Compton-scattering probability and a low atomic number to suppress the photoabsorption. For this purpose, the electron tracker of SMILE-2+ ETCC with a sensitive volume of $30 \times 30 \times 30 \text{ cm}^3$ is filled with an argon-based gas (Ar : CF₄ : iso C₄H₁₀; the pressure ratio = 95 : 3 : 2) at a pressure of 2 atm. The approximate drift velocity of the electrons in this gas is $3.7 \text{ cm } \mu\text{s}^{-1}$. As the ETCC needs three-dimensional (3D) precise electron tracks for the gamma-ray reconstruction, we adopted a time-projection chamber (TPC) with a micro-pixel chamber (μ -PIC; Ochi et al. 2001; Takada et al. 2005) and a gas electron multiplier (Sauli 1997; Tamagawa et al. 2006) insulated by $100 \mu\text{m}$ liquid crystal polymer. To reduce the power consumption, we combined two adjacent readout strips of μ -PIC into one preamplifier. The readout pitch of the tracker is $800 \mu\text{m}$ and the energy resolution of the tracker through the whole volume is 45.9% for 0.043 MeV (GdK α) at the full width at half maximum (FWHM).

As the gamma-ray absorber, we selected GSO (Gd₂SiO₅:Ce) pixel scintillator arrays (PSAs), each containing 8×8 pixels. The pixel size is $6 \times 6 \text{ mm}^2$. The GSO scintillator is 26 and 13 mm thick at the bottom and sides of the electron tracker, respectively. To efficiently absorb the scattered gamma-rays, we placed 36 PSAs at the bottom and 18 PSAs at each side of the tracker. The total number of scintillation pixels was 6912. For the photo readout, we adopted the four-channel (ch) charge division method with a resistor network (Sekiya et al. 2006) and multi-anode photomultiplier tubes (Hamamatsu Photonics,

flat-panel H8500). The energy resolutions of the bottom and side PSAs for 0.662 MeV are 13.4% and 10.9%, respectively, at FWHM. The PSAs are placed in the TPC vessel, whereas the scintillators of the previous ETCC (SMILE-I) were placed outside of the vessel. The total number of readouts of TPC and PSAs is 768 ch for TPC and 432 ch, respectively. SMILE-2+ employs the same data-acquisition system as the medium-size ETCC prototype (Mizumoto et al. 2015), but with the VMe bus replaced by a gigabit ethernet link for fast data transference. The top of the TPC vessel is installed with a 5 mm thick plastic scintillator to reduce the number of triggers by charged particles.

The SMILE-2+ ETCC is set above the control system, as shown in Figure 2. The control system includes a central processing unit (CPU) for communication with the balloon control system, two CPUs with 1 TB solid-state drives for data acquisition, the trigger control unit described in Mizumoto et al. (2015), four high-voltage units for the TPC, a power management system with DC/DC converters, and lithium batteries. SMILE-2+ also has a receiver with a global positioning system, an atmospheric pressure gauge, two clinometers, and three geomagnetic aspectmeters (GAs) to measure the gondola attitude. However, it lacks a feedback system for attitude control. The accuracy of the posture measurements is lower than 5° . The total power consumption is approximately 250 W. Power is provided by the lithium batteries. The SMILE-2+ system is sealed in a pressured vessel maintained at 1 atm. The side of the outer vessel is covered by multilayered insulators for temperature maintenance, and the outer vessel is placed on the small aluminum gondola, as shown in Figure 3. The outer vessel is installed with an independent piggyback sensor (Shoji 2019) that measures the attitude with three GAs, three accelerometers, and a gyroscope. The gondola attitudes determined by the SMILE-2+ sensors and the piggyback sensor were checked for consistency. Without ballast, the SMILE-2+ gondola weighs 511 kg in total.

2.2. Ground Calibration

The gaseous electron tracker on the ETCC obtains the 3D tracks and energies of the Compton-recoil electrons, whereas the absorber detects the absorption points and energies of the Compton-scattered gamma-rays. The momentum of the incident gamma-rays is then obtained by summing the momenta of the recoil electrons and the scattered gamma-rays,

$$p_0^\mu = p_\gamma^\mu + p_e^\mu, \quad (1)$$

where p_0^μ , p_γ^μ , and p_e^μ are the four-dimensional momenta of the incident gamma-ray, scattered gamma-ray, and recoil electron, respectively. Using the measured values, the unit vector of the incident gamma-ray \mathbf{r} is described by

$$\mathbf{r} = \left(\cos \phi - \frac{\sin \phi}{\tan \alpha} \right) \mathbf{g} + \frac{\sin \phi}{\sin \alpha} \mathbf{e}, \quad (2)$$

where \mathbf{g} and \mathbf{e} are unit vectors in the directions of the scattered gamma-ray and the recoil electron, respectively, in the laboratory system. α is the angle between the scattering and recoil directions (see Figure 1), and ϕ is the scattering angle,

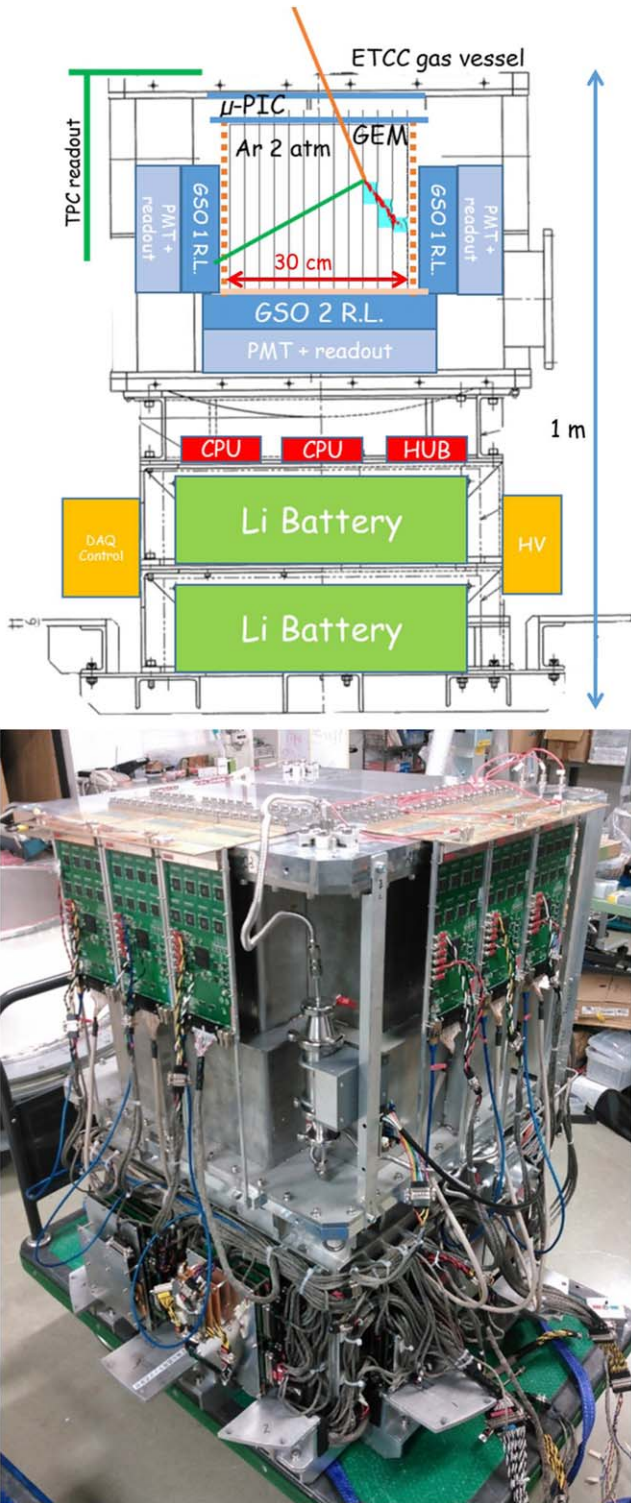


Figure 2. Cross-sectional view (upper) and photograph (lower) of the SMILE-2+ system. The upper and lower halves are the ETCC and the control system, respectively.

given by

$$\cos \phi = 1 - m_e c^2 \left(\frac{1}{E_\gamma} - \frac{1}{E_\gamma + K_e} \right). \quad (3)$$

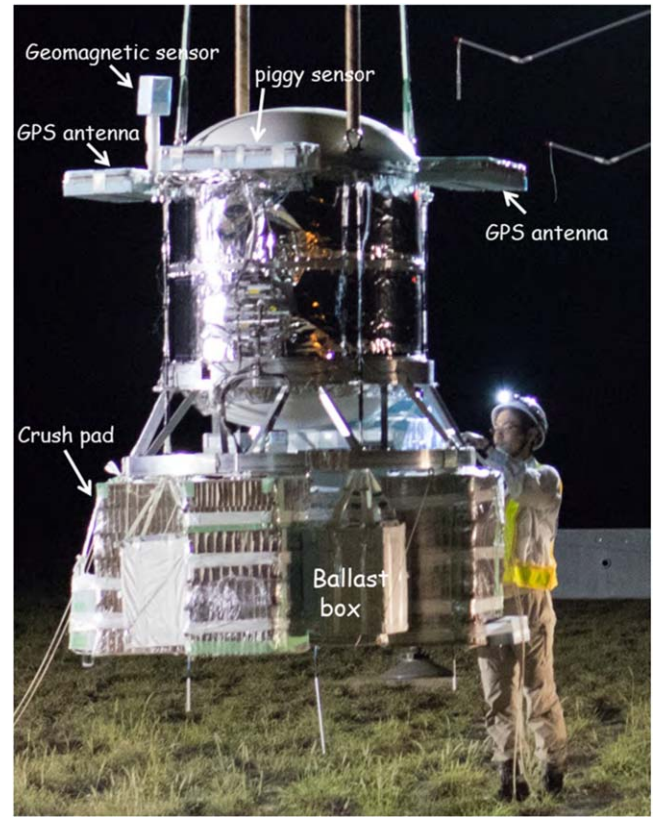


Figure 3. Photograph of the SMILE-2+ gondola.

In Equation (3), E_γ , K_e , m_e , and c denote the energy of the scattered gamma-rays, the kinetic energy of the Compton-recoil electrons, the electron mass, and the light speed, respectively.

The gamma-ray candidate events are reconstructed under the following criteria:

1. Single-pixel scintillator hits: When a Compton-scattered gamma-ray hits more than one pixel in the absorber, the incident gamma-ray is difficult to reconstruct because the sequence of interactions in the absorber becomes confused. Therefore we select only the events with a single-pixel scintillator hit.
2. Fully contained electrons: The gamma-ray reconstruction requires the kinetic energy of a recoil electron. If a recoil electron escapes the sensitive volume of the TPC, the incident gamma-ray cannot be reconstructed because the recoil energy measurement is incomplete. We thus set the TPC fiducial volume at $29 \times 29 \times 29 \text{ cm}^3$ and require that the track length matches the expected distance range of electrons depositing their energy in Ar gas (Tanimori et al. 2015). Figure 4 plots the track length of the charged particles detected in level flight versus the energy deposited in the TPC. The gradient in this figure represents the energy loss dE/dx . The events in the hatched area of this figure give rise to fully contained electrons. The head-tail of the recoil electrons is determined from the skewness of the track image (Dujmic et al. 2008) and the recoil direction is determined from the time-over-threshold information (Tanimori et al. 2015). The angular resolution of the recoil direction

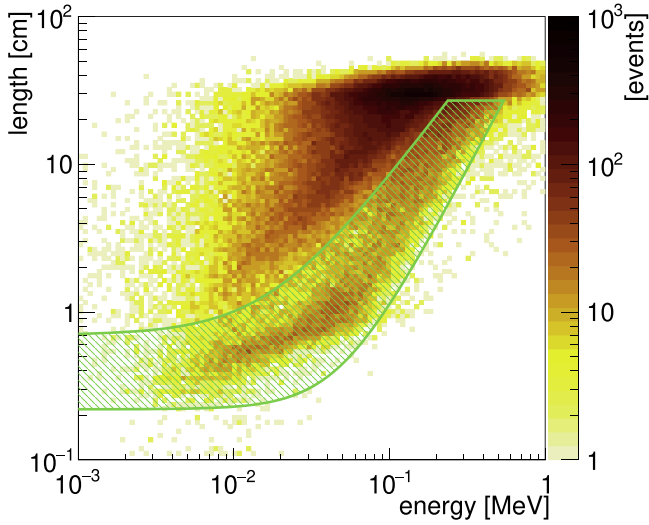


Figure 4. Track length of charged particles as a function of deposited energy in SMILE-2+ TPC. We selected only the fully contained electron events inside the hatched green area.

and the position resolution of the scattering points are determined by a traditional method (see Ikeda et al. 2021).

3. Compton-scattering kinematics: α is defined as

$$\cos \alpha_g = \mathbf{g} \cdot \mathbf{e}, \quad (4)$$

and can be calculated by Compton-scattering kinematics as follows:

$$\cos \alpha_k = \left(1 - \frac{m_e c^2}{E_\gamma}\right) \sqrt{\frac{K_e}{K_e + 2m_e c^2}}. \quad (5)$$

Therefore, we can select only Compton-scattering events with the condition described by

$$|\cos \alpha_g - \cos \alpha_k| \leq \Delta_\alpha, \quad (6)$$

where Δ_α is a cut parameter. For SMILE-2+ ETCC, we set $\Delta_\alpha = 0.5$.

The response function of parallel light, which is required to deconvolute the gamma-ray fluxes from celestial objects, was obtained in a simulator of SMILE-2+ ETCC based on Geant4 (version 10.04-patch02; Agostinelli et al. 2003). Electromagnetic interactions were calculated in G4EmLivermorePhysics while considering the Doppler broadening effect of Compton scattering. To confirm the reliability of the SMILE-2+ ETCC simulator, we measured the effective area, PSF, and energy resolution under irradiation by line gamma-rays from the checking sources placed approximately 2 m from the center of SMILE-2+ ETCC. The measured performances were compared with the simulated expectations. Figure 5 plots the effective areas as functions of incident energy when the checking sources were placed along the center axis of the ETCC or when parallel light was irradiated at a zenith angle of 0° . The expected and measured effective areas were consistent. In the energy-selected results, the realized effective area was 1.1 cm^2 at 0.356 MeV , which satisfies the criterion for detecting the Crab Nebula. The difference between all reconstructed events and the energy-selected events (twice the FWHM of the full-energy peak) increased at higher energies. This difference is caused by the scattered component,

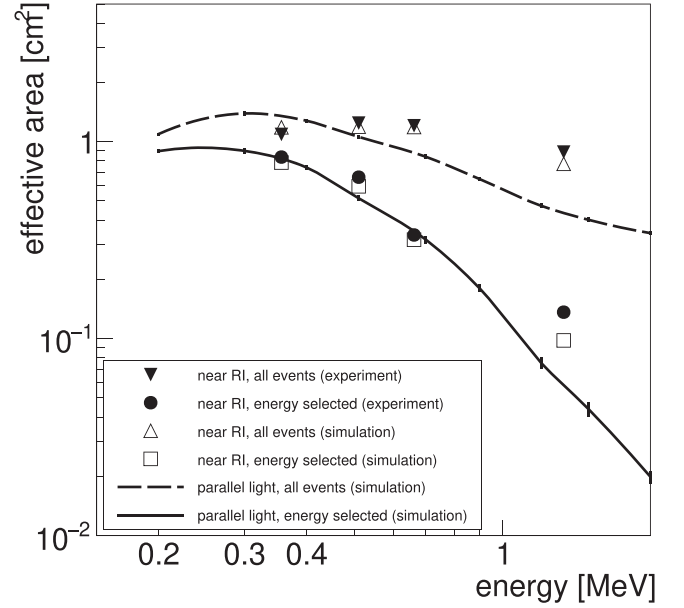


Figure 5. Effective areas as functions of incident energy. Filled and open triangles represent the effective areas of all reconstructed events obtained in the experiments and simulation, respectively. Filled circles and open squares represent the experimental and simulated effective areas after selection within the FWHM of the energy peak, respectively. Dashed and solid lines plot the effective areas of all events and energy-selected events in the parallel light case, respectively.

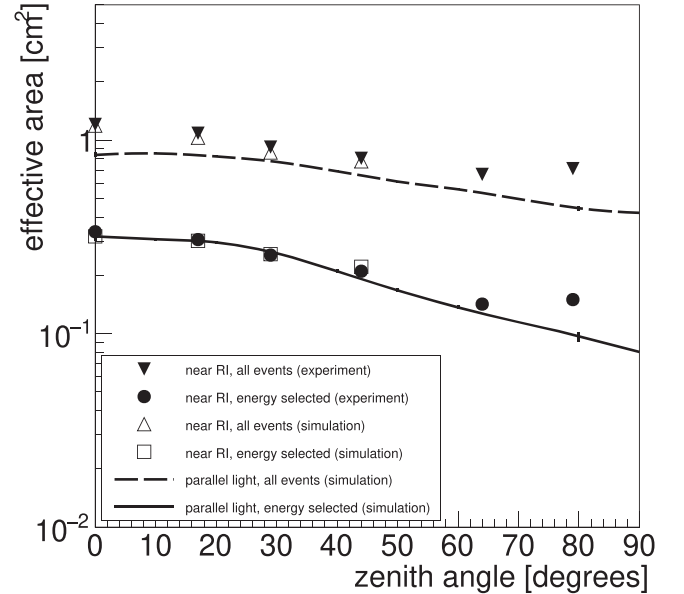


Figure 6. Zenith-angle dependence of the effective area at an incident energy of 0.662 MeV . Symbols are described in the caption of Figure 5.

namely, the scattered gamma-rays in the surrounding materials (e.g., the pressured vessel, TPC vessel, and PSA support structures) before the radiation enters the ETCC. As the major interaction between incoming rays and materials is Compton scattering, observations are considered to be confused not only by PSF blurring of the surrounding sources (the expected contamination), but also by components scattered from the structures. Therefore, an accurate response function is critical to obtain the true fluxes of celestial objects. The zenith-angle dependence of the effective area at 0.662 MeV is shown in Figure 6. As mentioned above, SMILE-2+ ETCC has a large

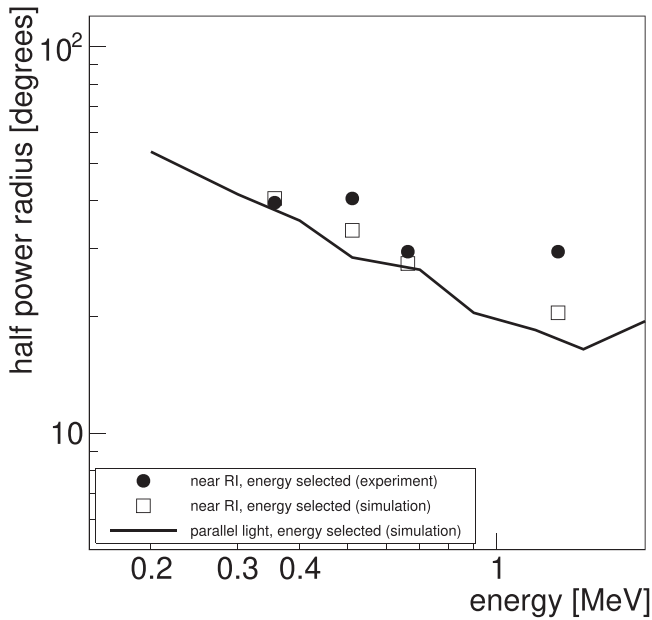


Figure 7. Half-power radius (HPR) of the PSF as a function of incident energy. The filled circles, open squares, and solid line represent the measured HPR using the checking sources, the simulated HPR with a near point source, and the simulated HPR for parallel light, respectively.

FoV (3.1 sr). This FoV is defined as the field covering more than half the effective area at the zenith. In the ETCC simulator, the accuracy of the effective area was better than 10% over the energy range 0.15–2.1 MeV within the FoV. Figure 7 plots the half-power radius (HPR) of the PSF as a function of incident energy. The PSF size of SMILE-2+ ETCC is 30° at the HPR for 0.662 MeV. Furthermore, the angular resolution measure (ARM) and scatter plane deviation (SPD) at the FWHM for 0.662 MeV, which define the accuracies of the scattering angle and the scattering plane, respectively, are $10^\circ.5$ and 148° for 0.662 MeV at the FWHM. The PSF of the ETCC depends on the energy resolution of the PSAs, the position accuracy of the Compton-scattering point, and the angular resolution of the direction of the Compton-recoil electrons. Although the SMILE-2+ ETCC has poorer spatial resolution than the advanced telescopes that observe other wavelengths, it satisfies the criteria for detecting the Crab Nebula with powerful background-rejection capability. Figure 8 shows the energy resolutions of SMILE-2+ ETCC, TPC, and PSA. The fully contained electron events are limited to recoil energies lower than 0.3 MeV because the TPC gas lacks any stopping power. Therefore the energy of the scattered gamma-ray exceeds that of the recoil electron, and the energy resolution of the ETCC is dominated by that of PSAs.

3. SMILE-2+ Balloon Flight

The SMILE-2+ balloon was launched by ISAS/JAXA from the Australian balloon launch station, Alice Springs, Australia, on 2018 April 7. Three hours before launch at 06:24 Australian Central Standard Time (ACST), the SMILE-2+ system was switched on; the data acquisition was running even during the ascent. The time variations of the altitude and atmospheric pressure are shown in the upper and lower panels of Figure 9, respectively. At 08:44 ACST, the balloon reached an altitude of 39.6 km. SMILE-2+ performed observations until 10:45 ACST on 2018 April 8, and was switched off at 10:53 ACST. At

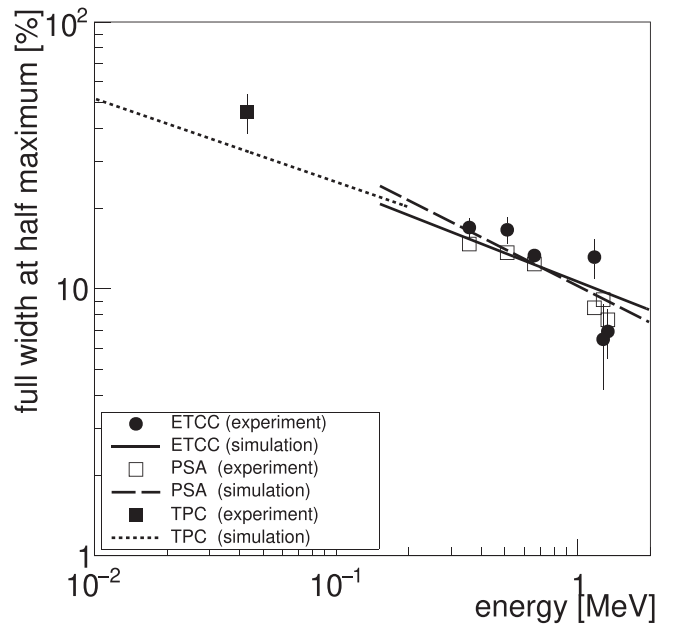


Figure 8. Energy resolutions of the ETCC, TPC, and PSAs as functions of energy. The filled circles and solid line represent the energy resolutions of the SMILE-2+ ETCC obtained via ground calibration and simulation, respectively. The filled and open squares are the averaged energy resolutions of the TPC and PSAs, respectively, measured via ground calibration. The dotted and dashed lines represent the simulated energy resolutions of TPC and PSA, respectively.

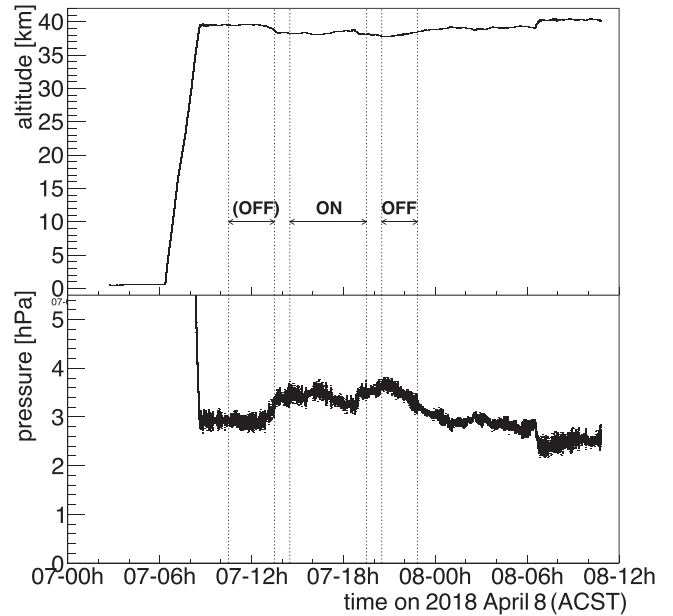


Figure 9. Time variations of the altitude of SMILE-2+ gondola (upper panel) and atmospheric pressure (lower panel). During the ‘ON’ period, Crab Nebula was included in the FoV and was observed. ‘OFF’ and ‘(OFF)’ denote the period of the background modeling when the atmospheric depth was the same and thinner than that of during the ON periods, respectively. During these periods, the Crab Nebula was excluded from the FoV of SMILE-2+.

06:30 ACST on 2018 April 8, the balloon slightly ascended owing to sunrise. The duration of the level flight, in which the atmospheric depth was maintained between 2.4–3.8 hPa (altitude 37.8–40.4 km), was approximately 26 hr. On 2018 April 9, we approached and successfully recovered the SMILE-2+

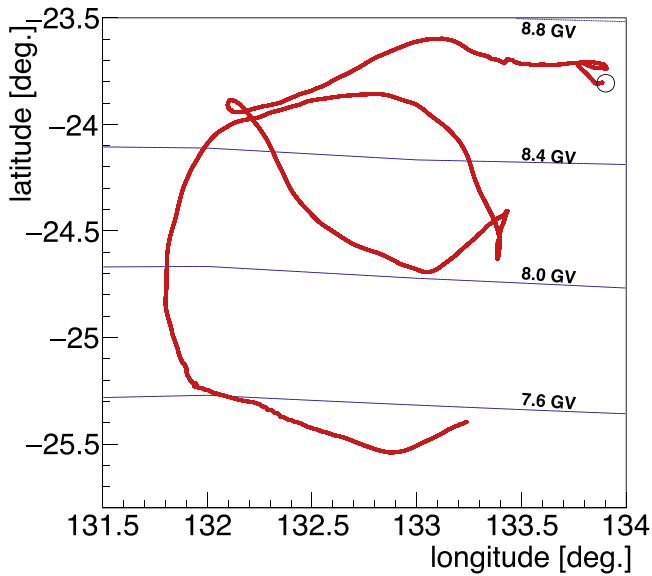


Figure 10. Flight path of SMILE-2+. The open circle represents the position of the Australian balloon launch station, and the contours outline the cutoff rigidity calculated by PARMA (Sato et al. 2008).

gondola, which had landed approximately 190 km from Alice Springs.

Figure 10 shows the flight path of the SMILE-2+ balloon from the launch time until turn-off of the SMILE-2+ system. The cutoff rigidity (marked by the contours in Figure 10) was calculated by PARMA (Sato et al. 2008) based on MAGNETOCOSMICS (Deaorgher et al. 2005). The time-averaged cutoff rigidity was 8.2 ± 0.4 GV during the level flight, and the K_p index, which indicates an indicator of the disturbances in the Earth’s magnetic field, was below 2.⁷ The low K_p index confirmed a stable and quiescent magnetic field condition, under which the intensities of cosmic rays should cause negligible fluctuations in the SMILE-2+ observation. In contrast, the intensity of atmospheric gamma-rays is proportional to $zR_{\text{cut}}^{-1.13}$ (Schönfelder et al. 1977; Thompson et al. 1981), where z and R_{cut} are the atmospheric depth and the cutoff rigidity, respectively. Between 13:32 and 23:00 ACST on 2018 April 7 (see Figure 9), the balloon altitude decreased with a concomitant 20% increase in atmospheric depth. The intensity of atmospheric gamma-rays was expected to rise at this time.

The time variations of the elevation angles and air masses of the observation targets are shown in panels (a) and (b) of Figure 11, respectively. Panel (c) of this figure shows the count rates of PSAs (blue), TPC (magenta), and ETCC (red) as functions of time; (d) live time of the data acquisition; (e) light curve obtained after gamma-ray reconstruction and live time correction. This light curve is the total event rate of the final remaining gamma-rays in all direction. The hatched area in panels (b), (c), (d), and (e) represents the ascending period of the balloon.

⁷ <https://www.gfz-potsdam.de/en/kp-index>

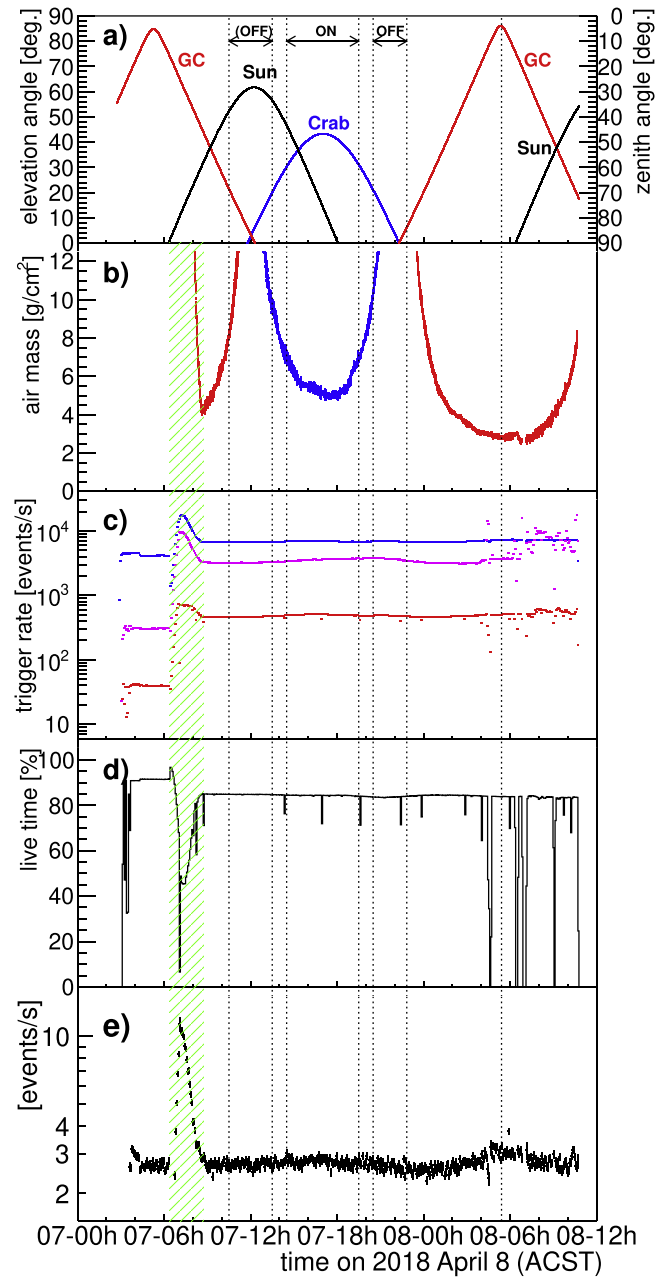


Figure 11. Time variations of (a) elevation angles and (b) air mass during the SMILE-2+ experiment. Red, blue, and black represent the Galactic center, the Crab Nebula, and the Sun, respectively. (c) Count rates of PSAs (blue), TPC (magenta), and ETCC (red) as functions of time; (d) live time of the data acquisition; (e) light curve obtained after gamma-ray reconstruction and live time correction. This light curve is the total event rate of the final remaining gamma-rays in all direction. The hatched area in panels (b), (c), (d), and (e) represents the ascending period of the balloon.

Figure 12 represents the exposure map with the definition of the observation area by the zenith angle below 60° .

4. Analysis

4.1. Gamma-ray Reconstruction

SMILE-2+ ETCC recorded 4.9×10^7 events after turn-on. Typical tracks detected during level flight are shown in Figure 13. Single-electron events were selected for the gamma-ray reconstruction as described in Section 2.2. The measured track images clearly showed the occurrences in

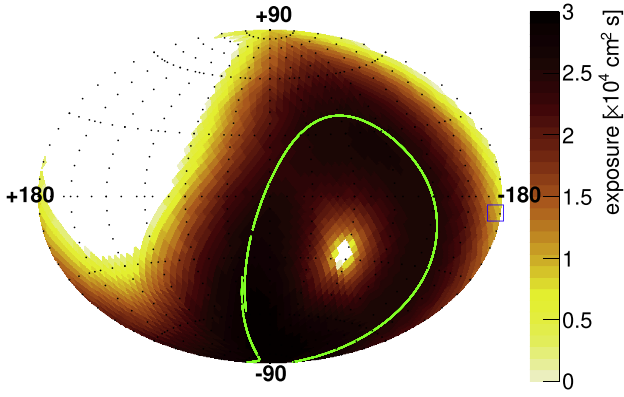


Figure 12. Exposure map of 0.3 MeV at zenith angles smaller than 60° (in galactic coordinates). The solid line represents the tracked light axis of SMILE-2+ ETCC, and the open square indicates the Crab Nebula.

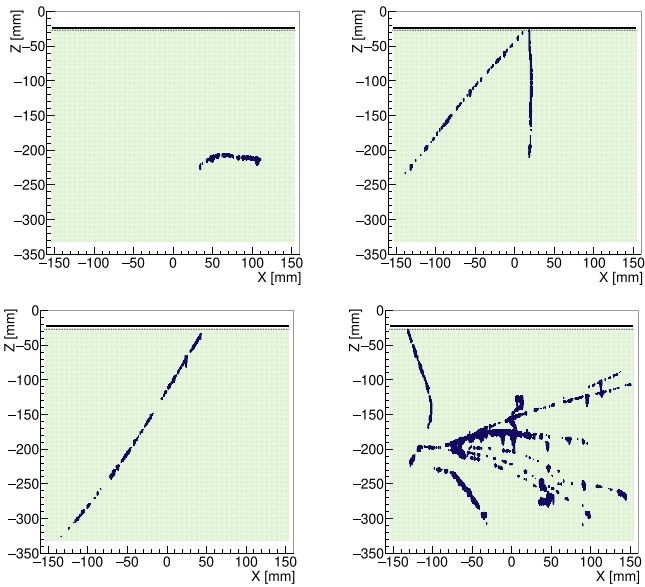


Figure 13. Typical tracks obtained by SMILE-2+ in the level flight. (top left: single-electron event, top right: pair-production event, bottom left: cosmic-ray event, bottom right: shower event) The hatched area represents the active volume of the TPC, and the upper and lower sides of each image represent the zenith and nadir directions, respectively.

SMILE-2+ ETCC from which select single-electron events were selected. Thus, the track image itself provides a simple and powerful means of noise suppression. At balloon altitudes, cosmic rays interact with the structural materials to produce positrons or gamma-rays. Because the ETCC is triggered by coincident PSAs and TPC, many cosmic-ray-induced events, including the electron-positron annihilation line absorbed in PSA, were recorded. Using the cosmic-ray or shower events in the flight data, we corrected the gain of the scintillators by the annihilation line every 30 minutes and the TPC gain by the energy deposition rate of the minimum ionizing particles every 10 minutes. Figure 14 shows the energy spectrum of each event selection during level flight, and the spectrum obtained by selecting all events, when 2.4×10^5 events remained. After selecting the fully contained electrons, the spectrum showed a clear excess at 0.511 MeV.

Figure 11 (e) shows the light curve obtained by the gamma-ray reconstruction in all directions with the live time correction. The gamma-ray event rate in all directions was $2.7 \text{ events s}^{-1}$

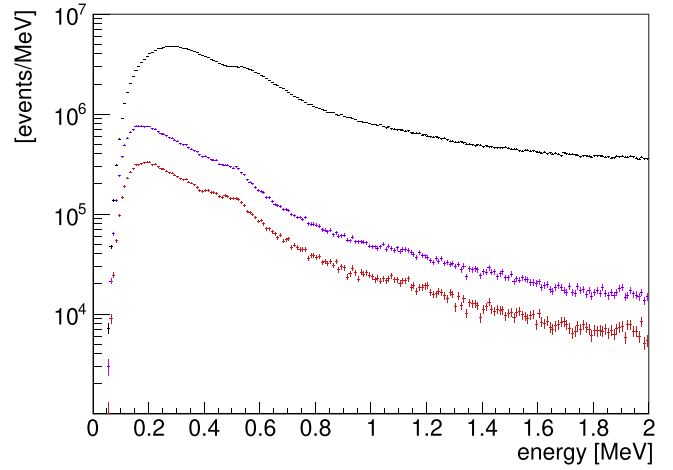


Figure 14. Total energy spectrum of each event selection during level flight (see Section 2.2 for details). The black and magenta spectra were taken after selecting single-pixel scintillator hits and fully contained electrons, respectively, and the red spectrum was obtained by Compton-scattering kinematics.

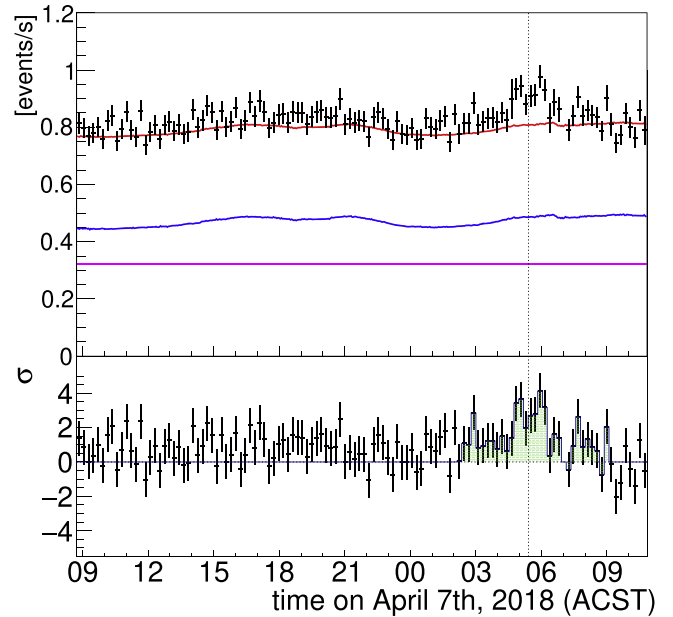


Figure 15. Light curve in the 0.15–2.1 MeV energy band at zenith angles below 60° during level flight. The vertical dotted line is the culmination time of the Galactic center. The blue curve describes the expected event rate when SMILE-2+ detected extragalactic diffuse and atmospheric gamma-rays. The magenta curve is the simulated background event rate induced by protons, neutrons, electrons, and positrons. The red line describes the total estimated event rate of SMILE-2+. The lower panel shows the difference between the observed and expected event rates. Within the hatched area, the air mass of the Galactic center was lower than 4 g cm^{-2} .

and remained stable during level flight. When the air mass of the Galactic center is lower than 4 g cm^{-2} , the light curve rises with increasing elevation angle of the Galactic center. The excess at the culmination time of the Galactic center is $0.5 \text{ events s}^{-1}$, so the estimated intensity of the GCR is $\sim 0.15 \text{ photons s}^{-1} \text{ cm}^{-2} \text{ sr}^{-1} \text{ MeV}^{-1}$ with an effective area of 1.1 cm^2 and FoV of 3.1 sr. The intensity result is roughly consistent with the intensity measured by SPI/INTEGRAL (Bouchet et al. 2011).

Figure 15 shows the light curve at zenith angles below 60° in the 0.15–2.1 MeV energy band. Plotted are the expected event rate at which SMILE-2+ detects the extragalactic diffuse and

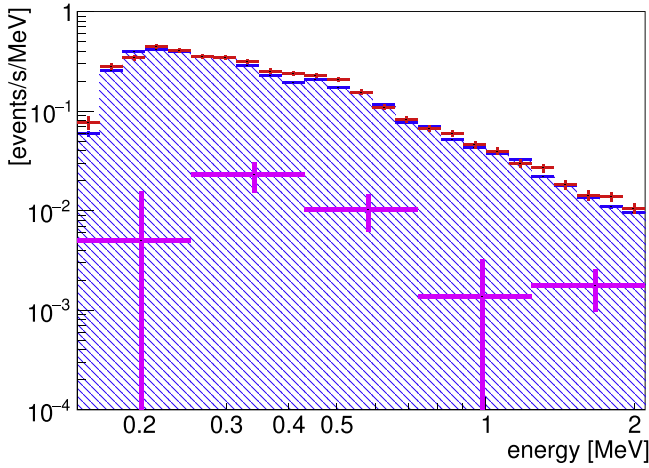


Figure 16. Observed energy spectrum of the ON-region (red), estimated background (hatched area, see text), and the subtraction (magenta).

atmospheric gamma-rays (blue curve) and the expected instrumental background event rate induced by protons, neutrons, electrons, and positrons (magenta line) that was calculated by PARMA (Sato et al. 2008) and Geant4. The intensity of atmospheric gamma-rays depends on the atmospheric depth, cutoff rigidity R , and solar modulation. Here, we adopted the semiempirical model by Ling (1975) to the atmospheric depth dependence of extragalactic diffuse and atmospheric gamma-rays. We additionally assumed that the intensity of atmospheric gamma-rays is proportional to $1.2R^{-1.13}$, as detailed in Section 5. The red line in Figure 15 plots the total event rate of SMILE-2+, estimated independently of the observation results. Over most of the level flight period, the observed rate 0.15–2.1 MeV events at a zenith angle of 60° is explained by the sum of extragalactic gamma-rays, atmospheric gamma-rays, and the instrumental background. The differential between the obtained and estimated event rates (lower panel of Figure 15) shows a significant excess around the culmination time of the Galactic center. The detector count rates of SMILE-2+ clearly reveal an enhanced gamma-ray emission from the GCR. In contrast, no clear excess appeared in Figure 11 (e) when the Crab Nebula was observed. This absence is explained by the low flux of the Crab Nebula (only $\sim 3\%$ of the photon number of extragalactic diffuse gamma-rays in the FoV of the ETCC in the energy range 0.2–2.1 MeV). In the ON-region of the Crab Nebula observation, we considered that the Crab Nebula ($l=184^\circ 6$, $b=-5^\circ 8$) was centered in a circle of radius 40° , which defines the HPR of the PSF at 0.3 MeV. The spectrum obtained in the ON-region is the red spectrum in Figure 16.

4.2. Background Estimation

In celestial gamma-ray observations at balloon altitudes, the gamma-ray background comprises extragalactic diffuse gamma-rays, atmospheric gamma-rays, and instrumental gamma-rays. Although extragalactic diffuse gamma-rays are isotropic at the top of the atmosphere, they are scattered and attenuated in the atmosphere at balloon altitudes. The intensities of atmospheric gamma-rays and the instrumental gamma-rays depend on the atmospheric depth, zenith angle, and intensity of cosmic rays. Unfortunately, the atmospheric depth increased by 20% during observations of the Crab Nebula. We thus defined an OFF-period of 20:30–22:50 ACST

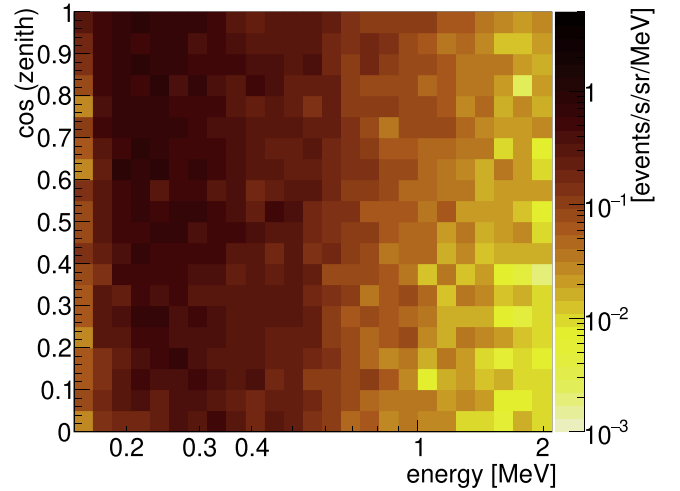


Figure 17. Event intensity map $B(E', \theta')$ in the detected energy E' vs. zenith angle θ during the OFF-period.

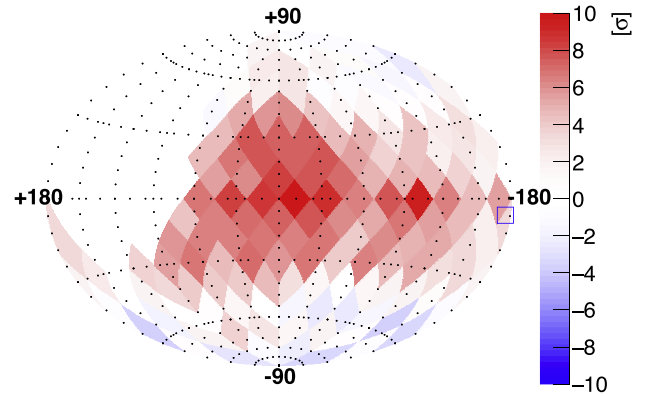


Figure 18. Significance survey map in galactic coordinates. The open square represents the Crab Nebula.

on 2018 April 7, when the balloon altitude decreased over the Crab observation period (Figure 9) and no bright celestial objects appeared inside the FoV. Figure 17 maps the event intensity $B(E', \theta')$ on the detected energy E' versus zenith angle θ' plane during the OFF-period. This event intensity map was assumed as the sky image of background gamma-rays in horizontal coordinates. Because the zenith angle of the ON-region varied over time, we calculated the average background energy spectrum $g(E')$ over the Crab observation period,

$$g(E') = \frac{1}{T_{\text{obs}}} \int_{\text{ON-region}} B(E', \theta'(t)) d\Omega dt, \quad (7)$$

where T_{obs} is the live time of the Crab observation period (hatched spectrum in Figure 16). After subtracting the estimated background $g(E')$ from the ON-region events, we obtained $f(E')$, the energy spectrum of gamma-rays from the Crab Nebula. The magenta spectrum in Figure 16 displays $f(E')$ as a function of E' . The convolved significance is 4.0σ . Applying the same method to the observed data from 08:44 ACST on 2018 April 7 to 06:30 ACST on the following day, we calculated the significance map shown in Figure 18. Because the balloon altitude varied in time, we defined $g(E')$ in two time periods: from 10:30 to 13:30 ACST on 2018 April 7, when the atmospheric depth was lower than 3.1 g cm^{-2} , and

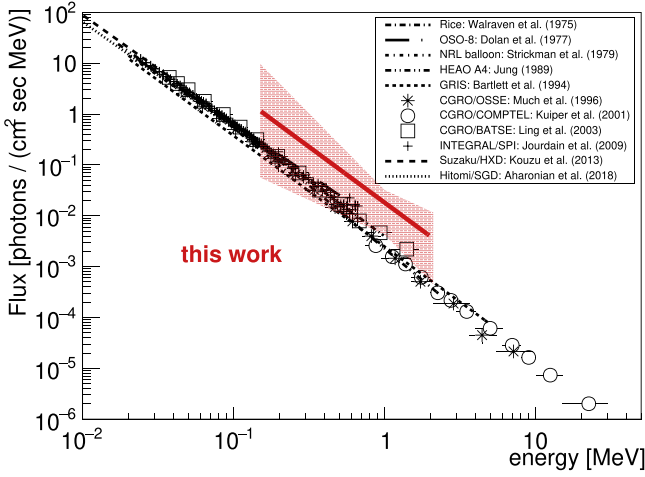


Figure 19. Photon flux spectrum of the Crab Nebula. The solid line and hatched area are the best-fit and statistical error region (1σ), respectively, obtained by SMILE-2+. The past observations of Rice (Walraven et al. 1975), OSO-8 (Dolan et al. 1977), NRL balloon (Strickman et al. 1979), HEAO A4 (Jung 1989), GRIS (Bartlett et al. 1994), OSSE/CGRO (Much et al. 1996), COMPTEL/CGRO (Kuiper et al. 2001), BATSE/CGRO (Ling & Wheaton 2003), SPI/INTEGRAL (Jourdain & Roques 2009), HXD/Suzaku (Kouzu et al. 2013), and SGD/Hitomi (Aharonian et al. 2018) are also shown in this figure.

from 20:30 to 22:50 ACST on 2018 April 7, when the atmospheric depth exceeded 3.1 g cm^{-2} . In addition to the light curve, SMILE-2+ significantly detected the GCR. A detailed study of the GCR will be described elsewhere.

4.3. Calculation of the Flux

The background-subtracted spectrum in Figure 16 includes the detector response and attenuation by the atmosphere,

$$f(E') = \frac{1}{T_{\text{obs}}} \int f_c(E) A(E, \theta, E', \theta') \exp\left(-\frac{z\tau_{\text{tot}}}{\cos\theta}\right) dE d\theta, \quad (8)$$

where E and θ are the true energy and true zenith angle of the incident photons, respectively, A is the response matrix of the ETCC, and z , τ_{tot} , and f_c denote the atmospheric depth, cross section of total attenuation in the atmosphere, and photon flux of the celestial object, respectively. $A(E, \theta, E', \theta')$ can be estimated using the ETCC simulator described in Section 2.2. Because θ , θ' , and z are temporally variable in balloon observations, we calculated the time-averaged response matrix as follows:

$$\bar{R}_{ij} = \frac{1}{T_{\text{obs}}} \int A(E_i, \theta, E'_j, \theta') \exp\left(-\frac{z\tau_{\text{tot}}}{\cos\theta}\right) dt, \quad (9)$$

where i and j are integers denoting specific energy bins. The resultant spectrum is then described as

$$f(E'_j) = \sum_i \bar{R}_{ij} f_c(E_i), \quad (10)$$

where f_c can be obtained through deconvolution. Assuming that f_c follows a single power law, the deconvolved photon flux was determined as $(1.82 \pm 1.40) \times 10^{-2} (E/\text{MeV})^{-2.19 \pm 0.82}$ photons $\text{s}^{-1} \text{cm}^{-2} \text{MeV}^{-1}$. This flux spectrum is shown in Figure 19 together with its 1σ error band. The Swift/BAT transient monitor (Krimm et al. 2013) revealed no significant

Table 1
Photon Flux Parameters Obtained in Different Background Periods

BG Time ^a	20:30–22:50	10:30–13:30	14:30–19:30
normalization ^b	1.82 ± 1.40	2.08 ± 1.38	1.55 ± 1.37
photon index	2.19 ± 0.82	2.28 ± 0.81	2.05 ± 0.80
significance	4.0σ	6.6σ	2.9σ

Notes.

^a time on 2018 April 7 in ACST

^b unit in 10^{-2} photons $\text{s}^{-1} \text{cm}^{-2} \text{MeV}^{-1}$

flares during the observation time.⁸ Therefore, as a consistency check, we can compare our result with other observations of the Crab Nebula. Our result is indeed consistent with previous observations of the Crab Nebula.

To investigate any time dependence of the OFF-period, we calculated the photon fluxes during two additional background periods: 10:30–13:30 ACST on 2018 April 7, and the Crab observation period. During the first of these periods, the atmospheric depth was 3.01 g cm^{-2} , 13% thinner than during the Crab observation period (14:30–19:30 ACST on 2018 April 7). Therefore, the intensity of atmospheric gamma-rays should decrease and the resulting gamma-ray flux of the Crab Nebula based on this background period should be over-estimated. The selection of the Crab observation period is justified because the Crab nebular flux is negligibly lower than the intensity of extragalactic diffuse and atmospheric gamma-rays within the ETCC FoV. The single power-law spectra within these additional two background periods were calculated as described for the original background period. The obtained parameters are listed in Table 1. As the parameters were quite similar in each case, the obtained photon flux depended little on the selection of the OFF-period.

5. Discussion

In general, the detection sensitivity $S(E)$ in some energy band is defined by the detectable flux with a significance of 3σ , an observation time of 10^6 s , and an energy window of $\Delta E = E$. The background rate and the detection sensitivity of SMILE-2+ are estimated by Equation (7) and by

$$S(E) = \frac{3\sqrt{T_{\text{obs}} \int B(E', \theta') dE' d\Omega'}}{T_{\text{obs}} \int A(E, 0^\circ, E', \theta') dE' d\Omega'}, \quad (11)$$

respectively, in the zenith direction ($\theta = 0^\circ$). When $d\Omega$ is defined by the HPR (see in Figure 7), the detection sensitivity of SMILE-2+ is the long-dashed blue line in Figure 20. The realized sensitivity, at which the Crab Nebula was detected within a few hours, was approximately 10 times better than that of SMILE-I.

The background events comprise extragalactic diffuse gamma-rays, atmospheric gamma-rays, instrumental gamma-rays, and other particles (e.g., neutrons). Radioactivation is negligible because the duration time is too short in balloon observation. Therefore the background event intensity $B(E', \theta')$ is described as

$$B(E', \theta') = \int (I_c + I_a) A(E, \theta, E', \theta') dE d\Omega + B_{\text{instr}}, \quad (12)$$

⁸ <https://swift.gsfc.nasa.gov/results/transients/index.html>

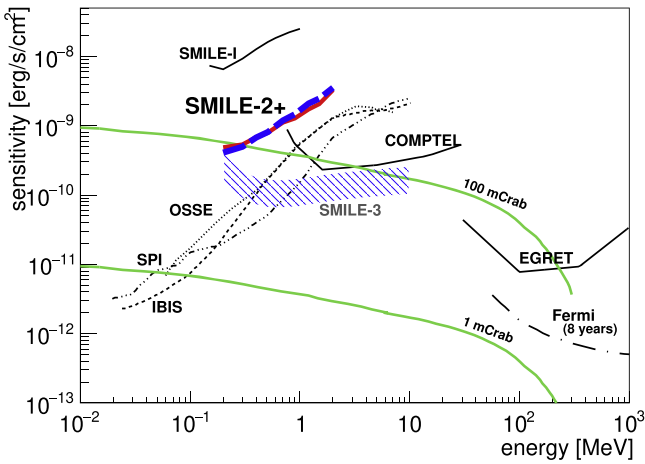


Figure 20. 3σ detection sensitivity of SMILE-2+ for the continuum spectrum at an observation time of 10^6 s within an energy window of $\Delta E = E$. The long-dashed blue line represents the realized sensitivity of SMILE-2+ based on the actual background event intensity. The solid red line plots the sensitivity of SMILE-2+ against the background photons comprising extragalactic diffuse gamma-rays, atmospheric gamma-rays, and the instrumental background. The hatched blue area represents the estimated detection sensitivity of the next observation (SMILE-3). The uncertainty in the SMILE-3 sensitivity depends on the cutoff rigidity, balloon altitude, and solar modulation. The black lines represent the results of previous studies (Attwood et al. 2009; Takahashi et al. 2013; Takada et al. 2011).

where I_c and I_a are intensities of extragalactic diffuse and atmospheric gamma-rays, respectively, and $B_{\text{instr}}(E', \theta')$ is the event intensity of the instrumental background. The intensity of extragalactic diffuse gamma-rays depends on the zenith angle and changes with atmospheric attenuation and scattering at balloon altitudes (Makino 1970; Horstman & Horstman-Moretti 1971; Schönfelder et al. 1977; Takada et al. 2011). In contrast, it is uniform at the top of the atmosphere. Atmospheric gamma-rays, produced when cosmic rays interact with the atmosphere, depend on the atmospheric depth, cutoff rigidity, and solar modulation. One of several models for atmospheric gamma-rays is PARMA (Sato et al. 2008), an analytical model based on PHITS simulations (Iwase et al. 2002). PARMA models the intensity of atmospheric gamma-rays with respect to energy, zenith angle, atmospheric depth, solar modulation, and cutoff rigidity, but does not consider the primary cosmic electrons/positrons as the initial particles. Ling (1975) and Ling et al. (1977) included extragalactic diffuse gamma-ray in a semiempirical model based on balloon observations. Their model considers the gamma-ray energy, zenith angle, and atmospheric depth, but does not consider the effect of cutoff rigidity and solar modulation on gamma-ray intensity. Nevertheless, this model is often cited in observational studies.

As the intensity model of extragalactic diffuse and atmospheric gamma-rays, we adopted the Ling (1975) and Ling et al. (1977) model and scaled by the dependences of cutoff rigidity and solar modulation. To correct the cutoff rigidity, we scaled the atmospheric component in the models by $4.5 \text{ GV}^{1.13}/8.4 \text{ GV}^{1.13}$. Meanwhile, the balloons referred to by Ling’s models were launched around solar maximum, whereas SMILE-2+ was launched near solar minimum. As the atmospheric gamma-ray intensity is about 1.2–2.0 times higher at solar minimum than at solar maximum (Morris 1984;

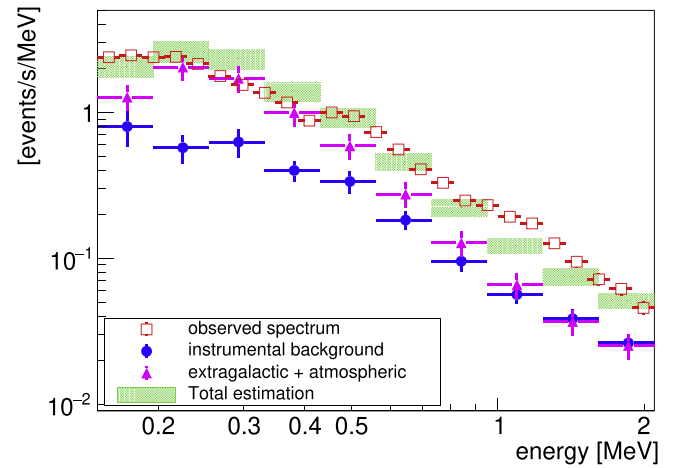


Figure 21. Energy spectra obtained within a zenith angle of 60° at an atmospheric depth of 3.0 g cm^{-2} . Open squares plot the events detected during 10:30–13:30 ACST on 2018 April 7. The filled circles, filled triangles, and hatched areas represent the estimated instrumental background, summation of the extragalactic diffuse and atmospheric gamma-ray components based on the Ling model (Ling 1975; Ling et al. 1977), and the total estimated spectrum, respectively.

Sazonov et al. 2007), we scaled the intensity of atmospheric gamma-rays by a factor of 1.2. Assuming a gamma-ray intensity at an atmospheric depth of 3.0 g cm^{-2} , we expected the SMILE-2+ ETCC spectrum represented by the filled triangles in Figure 21. To evaluate the instrumental background $B_{\text{instr}}(E', \theta')$, we simulated the reconstructed events of the ETCC simulator using the PARMA-calculated intensities of the initial particles (protons, neutrons, electrons, and positrons). The filled circles in Figure 21 describe the estimated energy spectrum of the instrumental background at the same altitude. The amount of instrumental background was one-half that of the essential background composed of extragalactic diffuse and atmospheric gamma-rays. Thus the instrumental background negligibly affected the detection sensitivity of SMILE-2+. The expected total background spectrum (indicated by the hatched area in Figure 21) approximately matched the observed energy spectrum (described by the open squares in Figure 21). Against this estimated total background, we can obtain the detection sensitivity independently of the sensitivities mentioned above. The estimated detection sensitivity of SMILE-2+ (solid red line in Figure 20) was also consistent with the realized sensitivity.

As confirmed in these results, the background spectrum and the detection sensitivity of observations by an ETCC in space are well embodied in the results of the ground calibrations. In contrast, the obtained sensitivities of COMPTEL and most of the other conventional Compton cameras are several times worse than the expected sensitivities (Schönfelder 2004; Bandstra et al. 2011). The above estimation is strongly and independently supported by the enhanced light curve at the culmination time of the Galactic center. If the instrumental background were several times more intense than the extragalactic gamma-rays, such as COMPTEL, this enhancement could not have been observed. The instrumental background of ETCC observations is mainly contributed by gamma-rays generated by interactions between cosmic rays and the instrumental material. Other disturbances are diminished or removed by powerful background-rejection tools such as particle identification, track image, and a Compton kinematics

test. The upward instrumental gamma-rays are intense because the instrumental material is below the ETCC. However, because the ETCC can pinpoint the direction of an incident gamma-ray to a point in each event, SMILE-2+ can suppress the instrumental background within the FoV to the expected contamination level of the PSF. Under this noise condition, the detection sensitivity of the next observation (SMILE-3) can be estimated both easily and reliably. After constructing a new TPC of volume $30 \times 30 \times 30 \text{ cm}^3$ filled with CF_4 gas at a 3 atm pressure and optimizing the structural design, the effective area of ETCC will be approximately 10 cm^2 for 0.4 MeV and 1 cm^2 for 2.5 MeV. To improve the PSF, we are developing an analysis method based on machine learning. In the first trial, deep learning of the recoil direction and scattering point improved the PSF to double that of the present paper (Ikeda et al. 2021). If the direction accuracy of Compton-recoil electrons could be improved to the limiting accuracy of multiple scattering, the PSF of the ETCC will improve to 10° and 2° at HPR for 0.4 MeV and 2.5 MeV, respectively. The sensitivity of an ETCC loaded on a long-duration balloon (SMILE-3) should exceed that of COMPTEL by several times (indicated by the hatched blue area in Figure 20). Recently, a superpressure balloon has been launched for over one month at medium latitudes in the southern hemisphere (Kierans et al. 2017). Therefore, if we can launch an updated ETCC on a long-duration balloon in the SMILE-3 mission, we could significantly surpass the COMPTEL observations because the large FoV of the ETCC enables observation times of $\sim 10^6 \text{ s}$.









6. Summary

To advance MeV gamma-ray astronomy, we are developing an ETCC with imaging-spectroscopy ability. The ETCC is based on bijection imaging and uses powerful background-rejection tools (particle identification, Compton-scattering kinematics test, and charged-particle track imaging). A proper PSF is performed on the celestial sphere, enabling acquisition of the energy spectrum of the observation target with a simple ON-OFF method. In 2018, we launched the second balloon (SMILE-2+) to confirm ETCC observations of celestial objects. The effective area of the ETCC loaded on SMILE-2+ is 1.1 cm^2 for 0.356 MeV, the PSF is 30° at HPR for 0.662 MeV, and the FoV is 3.1 sr when a $30 \times 30 \times 30 \text{ cm}^3$ TPC is filled with argon gas at 2 atm pressure. The observed flux and energy spectrum during the level flight, estimated independently of the experimental results, were well explained by a background of extragalactic diffuse, atmospheric, and instrumental gamma-rays. With this good understanding of the sensitivity and background, we achieved the prelaunch expectations (a significance level of 4.0σ) of SMILE-2+ observations of gamma-rays from the Crab Nebula. The obtained flux was also consistent with other flux observations. In addition, the light curve and the significance survey map show that the GCR is very bright, with a significance of $\sim 10\sigma$ in the 0.2–2.1 MeV energy range. Thus, SMILE-2+ is the first application of imaging spectroscopy based on a proper PSF and bijection imaging to MeV gamma-ray astronomy. The observed energy spectrum during level flight was explained by the background noise, which contains extragalactic diffuse, atmospheric, and instrumental gamma-rays. The achieved detection sensitivity of SMILE-2+ matched the sensitivity estimated from ground calibrations, whereas the sensitivities of most conventional Compton cameras are several times worse than their

expected values. The instrumental gamma-rays affected the detection sensitivity of SMILE-2+ little because they constituted only one-third of the background. For this reason, the ETCC overcomes the large background problem. When designing a Compton camera, the sensitivity must be estimated with a PSF (not an ARM), similarly to telescopes operating in the X-ray or GeV bands. In the near future, the ETCC will be updated to an approximate effective area of 10 cm^2 and a PSF of several degrees at the HPR, and we will then launch a long-duration balloon flight (SMILE-3) for scientific observations. The ETCC can become a unique pioneer with deeper survey ability than COMPTEL in MeV gamma-ray astronomy.

The balloon-borne experiment was conducted by Scientific Ballooning (DAIKIKYU) Research and Operation Group, ISAS, JAXA. This study was supported by the Japan Society for the Promotion of Science (JSPS) Grant-in-Aid for Scientific Research (S) (21224005), (A) (20244026, 16H02185), Grant-in-Aid for Young Scientists(B) (15K17608), JSPS Grant-in-Aid for Challenging Exploratory Research (23654067, 25610042, 16K13785, 20K20428), a Grant-in-Aid from the Global COE program “Next Generation Physics, Spun from Universality and Emergence” from the Ministry of Education, Culture, Sports, Science and Technology (MEXT) of Japan, and Grant-in-Aid for JSPS Fellows (16J08498, 18J20107, 19J11323). Some of the electronics development was supported by KEK-DTP and Open-It Consortium. And we thank Enago (www.enago.jp) for the English language review.

ORCID iDs

Atsushi Takada  <https://orcid.org/0000-0002-2515-5573>
 Yoshitaka Mizumura  <https://orcid.org/0000-0001-9213-0678>
 Kenji Hamaguchi  <https://orcid.org/0000-0001-7515-2779>
 Hidetoshi Kubo  <https://orcid.org/0000-0001-9159-9853>
 Shunsuke Kurosawa  <https://orcid.org/0000-0001-7873-4969>
 Kentaro Miuchi  <https://orcid.org/0000-0002-1546-7370>
 Tatsuya Sawano  <https://orcid.org/0000-0003-4462-0298>
 Toru Tanimori  <https://orcid.org/0000-0003-4427-0961>

References

- Agostinelli, S., Allison, J., Amako, K., et al. 2003, *NIMPA*, 506, 250
 Aharonian, F., Akamatsu, H., Akimoto, F., et al. 2018, *PASJ*, 70, 113
 Aprile, E., Curioni, A., Giboni, K. L., et al. 2008, *NIMPA*, 593, 414
 Attwood, W. B., Abdo, A. A., Ackermann, M., et al. 2009, *ApJ*, 697, 1071
 Bandstra, M. S., Belim, E. C., Boggs, S. E., et al. 2011, *ApJ*, 738, 8
 Bartlett, L. M., Barthelmy, S. D., Gehrels, N., et al. 1994, in *AIP Conf. Proc.* 304 (Melville, NY: AIP), 67
 Boggs, S. E., Lin, R. P., Slassi-Sennou, S., et al. 2000, *ApJ*, 544, 320
 Bouchet, L., Jourdain, E., Roques, J.-P., et al. 2008, *ApJ*, 679, 1315
 Bouchet, L., Strong, A. W., Porter, T. A., et al. 2011, *ApJ*, 739, 29
 Briggs, M. S., Band, D. L., Kippen, R. M., et al. 1999, *ApJ*, 524, 82
 Carr, B. J., Kohri, K., Sendouda, Y., & Yokoyama, J. 2010, *PhRvD*, 81, 104019
 Churazov, E., Sunyaev, R., Isem, J., et al. 2015, *ApJ*, 812, 62
 Deaorgher, L., Flückiger, E. O., Gurtner, M., Moser, M. R., & Bütikofer, R. 2005, *JMPA*, 20, 6802
 Diehl, R., Siebert, T., Greiner, J., et al. 2018, *A&A*, 611, 12
 Diehl, R., Siebert, T., Hillebrandt, W., et al. 2015, *Sci*, 345, 1162
 Dolan, J. F., Crannell, C. J., Dennis, B. R., et al. 1977, *ApJ*, 217, 809
 Dujmic, D., Tomita, H., Lewandowska, M., et al. 2008, *NIMPA*, 584, 327
 Hamaguchi, K., Tanimori, T., Takada, A., et al. 2019, *BAAS*, 51, 145
 Horstman, H., & Horstman-Morette, E. 1971, *Natur*, 229, 148
 Ikeda, T., Takada, A., Abe, M., et al. 2021, *PTEP*, 2021, 083F01

- Iwase, H., Niita, K., & Nakamura, T. 2002, *J. Nucl. Sci. Technol.*, 39, 1142
- Jourdain, E., & Roques, J. P. 2009, *ApJ*, 704, 17
- Jung, G. V. 1989, *A&A*, 338, 972
- Kamiya, K. 2011, Ph.D, University of California
- Kierans, C., Boggs, S., Chiu, J. L., et al. 2017, in 11th INTEGRAL Conf. Gamma-Ray Astrophysics in Multi-Wavelength Perspective (INTEGRAL2016) (Trieste: PoS), 075
- Kierans, C., Boggs, S. E., Zoglauer, A., et al. 2020, *ApJ*, 895, 44
- Kouzu, T., Tashiro, M. S., Terada, Y., et al. 2013, *PASJ*, 65, 74
- Krimm, H. A., Holland, S. T., Corbert, R. H. D., et al. 2013, *ApJS*, 209, 14
- Kuiper, L., Hermsen, W., Cusumano, G., et al. 2001, *A&A*, 378, 918
- Ling, J. C. 1975, *JGR*, 80, 3241
- Ling, J. C., Mahoney, W. A., Willett, J. B., et al. 1977, *JGR*, 82, 1463
- Ling, J. C., & Wheaton, Wm. A. 2003, *ApJ*, 598, 334
- Mahadevan, R., Narayan, R., & Krolik, J. 1997, *ApJ*, 486, 268
- Makino, F. 1970, *Ap&SS*, 8, 251
- Matz, S. M., Share, G. H., Leising, M. D., et al. 1988, *Natur*, 331, 416
- McConnell, M. L., Bennett, K., Bloemen, H., et al. 1996, *A&A*, 120, 149
- Mészáros, P., & Rees, M. J. 2010, *ApJ*, 715, 967
- Mizumoto, T., Matsuoka, Y., Mizumura, Y., et al. 2015, *NIMPA*, 800, 40
- Morris, D. J. 1984, *JGR*, 89, 10685
- Much, R., Harmon, B. A., Nolan, P., et al. 1996, *A&A*, 120, 703
- Ochi, A., Nagayoshi, T., Koishi, S., et al. 2001, *NIMPA*, 471, 264
- Prantzos, N., Boehm, C., Bykov, A. M., et al. 2011, *RvMP*, 83, 1001
- Sato, T., Yasuda, H., Niita, K., et al. 2008, *RadR*, 170, 244
- Sauli, F. 1997, *NIMPA*, 386, 531
- Sazonov, S., Churazov, E., Sunyaev, R., et al. 2007, *MNRAS*, 377, 1726
- Schönfelder, V. 2004, *NewAR*, 48, 193
- Schönfelder, V., Aarts, H., Bennett, K., et al. 1993, *ApJS*, 86, 657
- Schönfelder, V., Bennett, K., Blom, J. J., et al. 2000, *A&A*, 143, 145
- Schönfelder, V., Graser, U., & Daugherty, J. 1977, *ApJ*, 217, 306
- Sekiya, H., Hattori, K., Kubo, H., et al. 2006, *NIMPA*, 563, 49
- Shoji, Y. 2019, in XXXII Int. Sym. on Space Technology and Science (Berlin: Springer)
- Siegert, T., Boggs, S. E., Tomsick, J. A., et al. 2020, *ApJ*, 897, 45
- Strickman, M. S., Johnson, W. N., & Kurfess, J. D. 1979, *ApJ*, 230, L15
- Strong, A. W., Moskalenko, I. V., & Reimer, O. 2000, *ApJ*, 537, 763
- Takada, A., Hattori, K., Kubo, H., et al. 2005, *NIMPA*, 546, 258
- Takada, A., Kubo, H., Nishimura, H., et al. 2011, *ApJ*, 733, 13
- Takahashi, T., Uchiyama, Y., & Stawarz, Ł. 2013, *Aph*, 43, 142
- Tamagawa, T., Tsunoda, N., Hayato, A., et al. 2006, *NIMPA*, 560, 418
- Tanimori, T., Kubo, H., Miuchi, K., et al. 2004, *NewAR*, 48, 263
- Tanimori, T., Kubo, H., Takada, A., et al. 2015, *ApJ*, 810, 28
- Tanimori, T., Mizumura, Y., Takada, A., et al. 2017, *NatSR*, 7, 41511
- Thompson, D. J., Simpson, G. A., & Özel, M. E. 1981, *JGR*, 86, 1265
- Toma, K., Sakamoto, T., & Mészáros, P. 2011, *ApJ*, 731, 127
- Trombka, J. I., Metzger, A. E., Arnold, J. R., et al. 1973, *ApJ*, 181, 737
- Urry, C. M., & Padovani, P. 1995, *PASP*, 107, 803
- von Ballmoos, P. 1995, *ExA*, 6, 85
- Walraven, G. D., Hall, R. D., Meegan, C. A., et al. 1975, *ApJ*, 202, 502
- Weidenspointner, G., Varendorff, M., Oberlack, U., et al. 2001, *A&A*, 368, 347
- Zoglauer, A., et al. 2003, in Nuclear Science Symp. Conf. Records (Piscataway, NJ: IEEE), 1694